Influence of π-conjugated cations and halogen substitution on the optoelectronic and excitonic properties of layered hybrid perovskites

Joshua Leveillee,[1,2,*] Claudine Katan,[3] Liujiang Zhou,[2] Aditya D. Mohite,[4] Jacky Even,[5] Sergei Tretiak,[2] André Schleife,[1,6,7] and Amanda J. Neukirch[2,†]

[1]*Department of Materials Science and Engineering, University of Illinois at Urbana-Champaign, Urbana, Illinois 61801, USA*
[2]*Los Alamos National Laboratory, Los Alamos, New Mexico 87545, USA*
[3]*Univ Rennes, ENSCR, INSA Rennes, CNRS, ISCR - UMR 6226, F-35000 Rennes, France*
[4]*Department of Chemical and Bimolecular Engineering, Rice University, Houston, Texas 77006, USA*
[5]*Univ Rennes, INSA Rennes, CNRS, Institut FOTON - UMR 6082, F-35000 Rennes, France*
[6]*Frederick Seitz Materials Research Laboratory, University of Illinois at Urbana-Champaign, Urbana, Illinois 61801, USA*
[7]*National Center for Supercomputing Applications, University of Illinois at Urbana-Champaign, Urbana, Illinois 61801, USA*

Low-cost chemical engineering of two-dimensional layered hybrid halide perovskite structures allows for the design of hybrid semiconductor quantum wells with tailored room-temperature excitonic optical absorption, emission, and charge carrier transport properties. Here density functional theory and the Bethe-Salpeter equation are used to predict the electronic structure and optical response of layered perovskites with two representative single-ring conjugated organic spacers, ammonium-propyl-imidazole (API) and 2-phenethylammonium (PEA). The inorganic perovskite quantum well properties are further tuned by analyzing the effect of halogen ($X =$ I, Br, Cl) substitution. We found that visible light absorption occurs primarily within the perovskite layer and that UV light absorption induces partial electron-hole separation between layers. In addition, a strong exciton binding energy and influence on absorption spectrum is found by solving the Bethe-Salpeter equation. Our results suggest that further engineering is necessary beyond the single-ring limit, by introducing more conjugated rings and/or heavier nuclei into the organic spacer. This is a promising future direction to achieve photoinduced charge separation and more generally hybrid heterostructures with attractive optoelectronic properties.

I. INTRODUCTION

Three-dimensional (3D) hybrid organic-inorganic perovskites (HOPs) have rapidly emerged as some of the most promising thin-film photovoltaic materials [1–3]. Their allure comes from a combination of high photoconversion efficiency (PCE), low device processing cost due to low-temperature solution processing, and composition from earth-abundant and readily available materials. In particular, hybrid lead-halide perovskite (e.g., methylammonium lead iodide, MAPbI$_3$, and formamidinium lead iodine, FAPbI$_3$) solar cells have undergone a PCE increase from 3.5% to over 20% in about 5 years [4–6]. These devices have currently exceeded the certified record efficiency of multicrystalline Si cells [7]. Beyond photovoltaic applications, HOPs show potential in many other fields including hydrogen generation [8], x-ray and γ-ray detection [9–12], light emitting diodes (LEDs) [13], spintronics [14,15], and sensors [16]. Setting aside the issue of lead toxicity [17–22], the main impediment to industry deployment of perovskite devices is their instability to air, moisture [23], and light exposure [24,25].

Recently, *layered* HOPs (LHOPs) have reemerged as promising alternatives to their 3D counterparts. They have been suggested to be used as highly efficient white LEDs [26] and tunable optical detectors [27]. In these, quantum confinement effects within perovskite layers can be engineered and tailored to specific applications [28–31]. In particular, they are able to overcome some of the above-mentioned limitations [32–34], by offering much improved stability and decent photoconversion performance: Tsai *et al.* reported that nonencapsulated single crystals of *n*-butylammonium-methylammonium lead-iodine with $n = 3$ and 4 layers resist moisture-driven chemical degradation. They also showed that encapsulation of the crystals resulted in no chemical degradation under highly illuminated conditions, and built solar cells with a PCE of 12.5% with $n = 3$ and $n = 4$ layers [32]. The broad applications and variability of LHOPs have opened a field of research that is just beginning to produce deeply insightful and practically applicable results.

The LHOPs studied in this work fall into the Ruddlesden-Popper crystal class [35] and their characteristic structure consists of 2D layers of *n* corner-sharing metal-halide octahedra separated by, and ionically bonded to, large charged polyatomic cations (see Fig. 1). The inorganic perovskite layer can be tuned to a specific width of *n* octahedra or even cleaved along various planes, linking the octahedra in linear or zig-zag corrugated patterns [36–38]. Opportunities to engineer LHOPs not only originate from changing the inorganic perovskite stoichiometry, but also by choosing one or more of many complex large organic cations to separate the

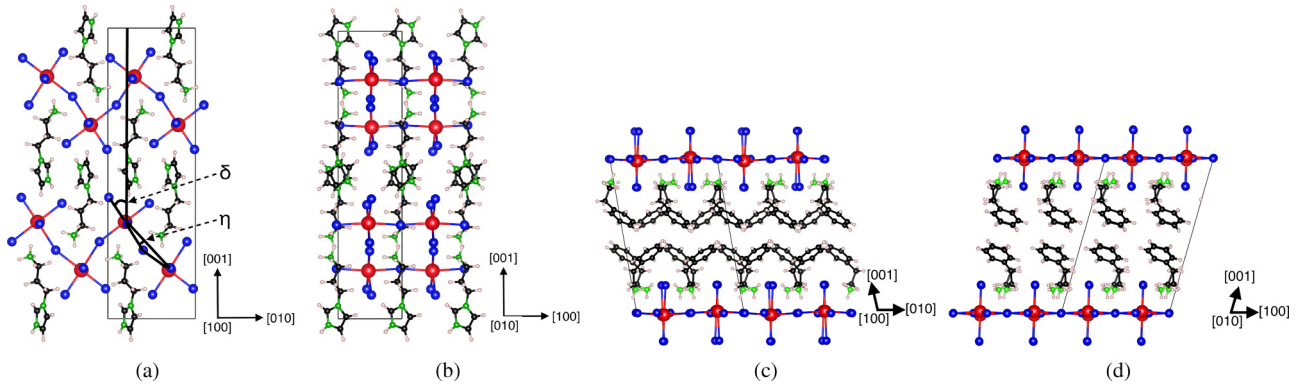*joshua.leveillee@gmail.com
†ajneukirch@lanl.gov

FIG. 1. The atomic structure of ammonium-propyl-imidizole (API)-PbBr$_4$ projected along the (a) [100] direction and (b) [010] direction and 2-phenethylammonium (PEA$_2$)-PbBr$_4$ projected along the (c) [100] and (d) [010] axes. The stacking direction is [001]. Atomic color coding: Pb (red), Br (blue), C (black), N (green), and H (pink). Tilting angle δ and bond angle η are indicated (see text).

layers [26,36–39]. Promising organic cations range from simple carbon chains with ammonium caps to large chromophore complexes [40–42]. These degrees of freedom allow for the exploration of a wide variety of electronic properties and the tuning of optical response.

In this context, optically activated charge separation between the organic and inorganic layers of LHOPs has been long sought to reduce the overlap between electron and hole wave functions and, thus, allow utilization of separated electron-hole channels for highly efficient charge transport. The advent of organic solar cells has proven that π-conjugated polymers are fully capable of producing and transporting bound electron-hole pairs (excitons) under illumination [43,44]. It has further been suggested that interchain charge separation of bound electron-hole pairs is possible in these systems [45]. Furthermore, charge transfer between semiconductor CdSe quantum dots and poly[2-methoxy-5-(2-ethyl-hexyloxy-p-phenylenevinylene)] bonded functional coatings has been observed [46]. This raises an interesting question whether organic layers in LHOPs with π-conjugated organic cations could similarly carry photocurrent under illumination if optical absorption excites electrons and holes that are localized in parallel layers of the LHOP system. If so, extensive chemical degrees of freedom in LHOPs could allow for engineering a layered organic-inorganic compound material that is capable of efficiently separating electrons and holes. These layers may provide separate conduction channels for electrons and holes, potentially reducing detrimental recombination. However, it is unknown how active the π-conjugated organic compounds in LHOPs are under ultraviolet-visible (UV-VIS) absorption, in particular in the stoichiometric limit of $n = 1$ perovskite layers between each organic layer.

To address this, Li *et al.* conclude from a large Stokes shift in the photoluminescence emission spectrum that charge separation occurs between the organic ammonium-propyl-imidizole (API) layer and inorganic PbBr$_4$ perovskite layer of [110] oriented API lead-bromide ($n = 1$) [47]. They also performed density functional theory (DFT) calculations and report an isolated carbon-π^* state in the fundamental band gap, to which they attribute the carrier separation and resulting massive Stokes shift. However, this material has not been studied by modern first-principles approaches that include the effects of spin-orbit coupling (SOC) and electron-hole

interaction on the optical-absorption spectrum. In particular, SOC has shown to be very important in determining the correct electronic band structure in Pb-containing hybrid perovskite materials [14,15,29,48]. Furthermore, several reasons for a large Stokes shift are debated and no conclusion has been reached: It has been suggested recently that it originates from strongly bound small-polaron states that form in the perovskite layer, lowering the emission energy of electron-hole pairs [49,50]. While the extent of octahedral tilting in and out of the perovskite plane has also been correlated with the magnitude of the Stokes shift [51,52], Du *et al.* found no such correlation from their analysis of the optical absorption and emission character of layered Pb(I, Br, Cl)$_4$ perovskites with acene alkylamine organic cation layers [53]. Hence, the debate to what extent π-conjugated organic layers participate in the optical absorption and emission of LHOPs is still open.

In the present study, we report first-principles calculations, for single π-conjugated LHOPs to determine the organic and inorganic layer contributions to electronic structure and optical absorption. We also clarify at what energies this becomes a significant contributor to the total optical response. The materials of interest are the $\langle 110 \rangle$ API-PbX_4 class ($X = $ I, Br, Cl) of layered perovskites, motivated by the work of Li *et al.* [47] and the single π-conjugated organic cation perovskites 2-phenyl-ethylammonium (PEA) PEA$_2$-PbX_4 ($X = $ I, Br, Cl) due to their readily available experimental atomic geometries and single π-conjugated (benzene) group per organic ion (see Fig. 1). We compute the ion-projected electronic structure and single-particle optical response using density functional theory (DFT), including spin-orbit coupling (SOC) and band gap corrections determined by HSE06 hybrid-functional calculations. The PBE+SOC+Δ_{HSE06} calculations reported in this work are an approximation of the full single-particle excitation energy calculations within the GW+SOC many-body perturbation theory formalism [54]. The two-particle optical response, which includes the effect of exciton formation, is calculated from the solution of the Bethe-Salpeter equation (BSE). Our results clarify energetic alignment of the bands associated with organic and perovskite components in both materials and provide detailed analysis of essential electronic wave functions and individual contributions to optical absorption spectra. This allows us to answer the question whether optical excitations occur within individual layers of single
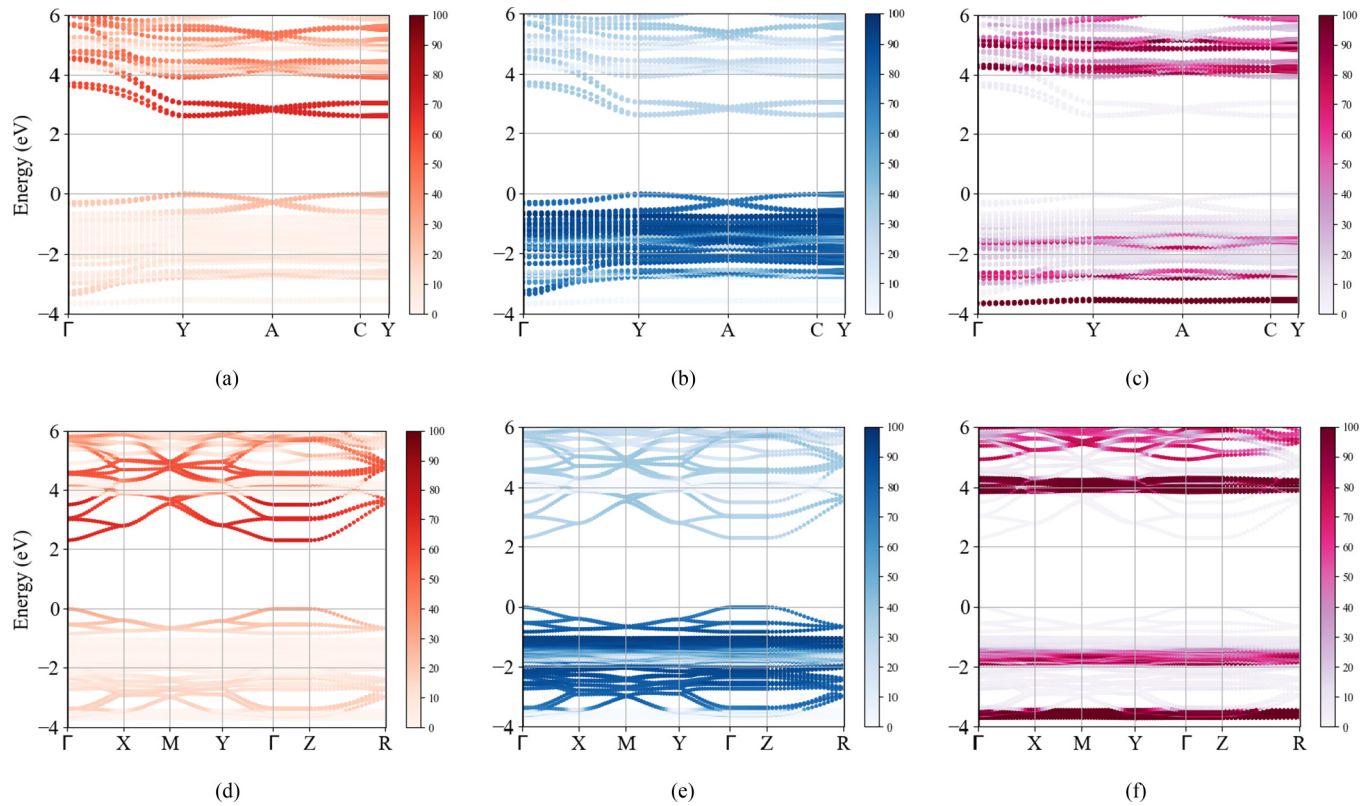
FIG. 2. The ion-projected band structures, computed using PBE+SOC+Δ_{HSE06}, of API-PbBr$_4$ (a)–(c) and PEA$_2$-PbBr$_4$ (d)–(f). The color bar indicates the contribution of Pb (red), Br (blue), and API/PEA (magenta) to each state as a percentage.

π-conjugated LHOPs or whether optical excitations partially separate electrons and holes between layers.

II. RESULTS

Atomic structure. The structure of single-layer $\langle 110 \rangle$ API-PbX_4 compounds resembles that of the $\langle 100 \rangle$ class of layered perovskites: The major difference is the corrugation of the perovskite layer with a zig-zag type octahedral linking in the $\langle 110 \rangle$ compounds and a linear-type linking in the $\langle 100 \rangle$ compounds. Figure 1 shows the [100] and [010] projections of both API-PbBr$_4$ and PEA$_2$-PbBr$_4$. PEA$_2$-PbX_4 experimental structures are used in our study [55–57]. Since experimental data are available only for API-PbBr$_4$ [47], we fully relax all API-PbX_4 atomic geometries in the $P2_1/c$ symmetry space group. The resulting lattice parameters and vector angles, unit-cell volumes, octahedron tilting angles, and Pb-X-Pb bond length ranges are reported in the Supplemental Material (SM) [58], Table S1, for all systems. The relaxed API-PbBr$_4$ atomic structure is in excellent agreement with the experimental structure determined by Li *et al.* [47], with errors of under 1% for lattice parameters, 0.2% for unit-cell volume, 1% for lattice vector angles, 2.5% for out-of-plane tilting, and 15% for in-plane tilting angles. The out-of-plane tilting angles δ_1 and δ_2 in the corrugated $\langle 110 \rangle$ API-PbX_4 systems should be $45°$, if no tilting is present. For the relaxed API-PbX_4 structures we find two distinct δ_1 and δ_2 in the ranges from $33.7°$ and $33.8°$ to $51.4°$ and $53.9°$, respectively.

In the linearly linked PEA$_2$-PbX_4 systems, $\delta = 0°$ under no tilting and indeed in the experimental structures, the out-of-

plane tilting angles remain small, in the range of $1°$ to $3°$. The in-plane-tilting angles, ranging between $\eta = 12.2°$ and $\eta = 14.5°$, are larger compared to those found in the API-PbX_4 systems, ranging from $\eta = 8.5°$ to $\eta = 10.5°$. This in-plane tilting is very similar to the octahedron tilting in orthorhombic MAPbX_3 3D HOPs [59].

Electronic structure. The band structures of API-PbX_4 and PEA$_2$-PbX_4 reveal dispersive band frontiers attributed to states localized on the perovskite as well as flat, nondispersive bands, situated more than 1 eV away from the band frontiers, that are attributed to the organic π and π^* states (see Fig. 2). Throughout the remainder of the paper, the label PBE+SOC+Δ_{HSE06} refers to the PBE+SOC band structure with conduction bands rigidly shifted to higher energy to match the HSE06+SOC band gap, and HSE06+SOC refers to fully noncollinear HSE06 hybrid-functional calculations that take SOC into account. Table I reports relevant calculated and experimentally determined energy gaps of these materials.

Ion-projected PBE+SOC+Δ_{HSE06} band structures are plotted for API-PbBr$_4$ in Figs. 2(a)–2(c). Similar data for the other API and PEA LHOPs considered in this work can be found in SM Figs. S2 and S3. Due to the $P2_1/c$ symmetry, the API-PbX_4 materials exhibit direct gaps of 2.10, 2.74, and 3.32 for API-Pb(I, Br, and Cl), respectively, at the Y point of the Brillouin zone (BZ). The Y point folds back to the Γ point when a 2×2 conventional cell is considered, as demonstrated by Pedesseau *et al.* [29]. The band gap we computed for API-PbBr4 using the HSE06 exchange-correlation functional with spin-orbit coupling underestimates the gap of 3.18 eV measured from the optical onset by Li *et al.* [47]. This can

TABLE I. Energy gaps (in eV) computed using different levels of theory. PBE+SOC+Δ_{HSE06} refers to the PBE+SOC electronic structure with the band gap rigidly shifted to the HSE06+SOC band gap value (see text).

Level of theory	API-PbI$_4$	API-PbBr$_4$	API-PbCl$_4$
PBE+SOC	1.44	1.94	2.41
HSE06+SOC	2.10	2.74	3.32
π-π^* gap (PBE+SOC+Δ_{HSE06})	5.87	5.88	5.7
BSE optical gap	1.74	2.23	2.68
Expt. optical gap [47]		3.18	
	PEA$_2$-PbI$_4$	PEA$_2$-PbBr$_4$	PEA$_2$-PbCl$_4$
PBE+SOC	1.33	1.75	2.12
HSE06+SOC	1.95	2.45	2.95
π-π^* gap (PBE+SOC+Δ_{HSE06})	5.39	5.82	5.53
Expt. optical gap [53]	2.45	3.0	3.6

be attributed to the fact that HSE06, albeit it improves over the DFT-PBE description, does not fully capture quasiparticle effects for the systems studied here. More sophisticated, but computationally more expensive methods, such as many-body perturbation theory, could mitigate these shortcomings [60]. Additionally, in this comparison the electron-hole interaction was neglected and, thus, the calculated electronic gap differs from the measured optical gap by the exciton binding energy. This will be discussed in the results for optical response. Differences between our relaxed structure and the experimental structure of API-PbBr$_4$ are expected to result in only small changes of the band gap, within 0.2 eV, based on the effects of in- and out-of-plane angles on gap values explored by Pedesseau *et al.* [29]. Figure 2 clearly shows that the band dispersion of API-PbBr$_4$ along the Y-Γ direction is free-electron-like, with a parabolic curvature near the Y point. Along the Y-A direction, the dispersion has a lower curvature, indicating a higher electron effective mass. Finally, along the Y-C direction the bands are effectively flat due to the layered and reduced periodicity of the LHOP crystals along the [001] direction. We observe the same trend for API-PbI$_4$ and API-PbCl$_4$.

In contrast, band structures of the PEA$_2$-PbX_4 LHOPs, with space groups $P2_1/c$, $P\bar{1}$, and $P\bar{1}$ for I, Br, and Cl, respectively, exhibit direct gaps of 1.95, 2.45, and 2.95 eV at the Γ point. The difference between the space groups of PEA$_2$-PbI$_4$ and PEA$_2$-Pb(Br, Cl)$_4$ is due to the bis-phenylethylammonium conformation of the chosen PEA$_2$-PbI$_4$ structure [53]. The general PEA$_2$ conformation explored by Du *et al.* assumed the same $P\bar{1}$ space group as the PEA$_2$-PbBr$_4$ and PEA$_2$-PbCl$_4$ systems. The band structure of PEA$_2$-PbBr$_4$, illustrated in Figs. 2(d)–2(f), exhibits highly dispersive, free-electron-like band frontiers along the Γ-X and Γ-Y directions, as well as flat, nondispersive band frontiers in the Γ-Z direction. Unlike the API-PbX_4 corrugated perovskites, the PEA$_2$-PbX_4 perovskites explored in this work are not corrugated in either in-plane direction. Thus, they have a higher periodicity in both in-plane lattice directions which manifests itself in highly dispersive band frontiers along two reciprocal-lattice directions. As a consequence, corrugated API-PbX_4 shows low effective-mass band frontiers only along Γ-Y, whereas PEA$_2$-PbX_4 shows low effective masses along both Γ-X and Γ-Y.

In traditional 3D HOPs such as MAPbX_3, valence and conduction band frontiers are composed of X:p+Pb:$6s$ and Pb:$6p$ states, respectively [61]. While, in principle, in the layered systems with conjugated organic cations explored in this work, API and PEA π and π^* states could contribute in the near-gap region, we find from the ion-projected band structure that the valence and conduction band frontiers are composed of X:p+Pb:$6s$ and Pb:$6p$ states, respectively. This is very similar to the 3D MAPbX_3 HOPs. However, unlike 3D MAPbX_3 HOPs that have organic states far below (about 6 eV) and above the band frontiers [61], API-PbX_4 and PEA$_2$-PbX_4 have flat, nondispersive bands attributed to API and PEA$_2$ π and π^* orbitals within 1.0 to 2.0 eV of the band frontiers, as shown in Fig. 2.

Furthermore, due to the strong contributions of Pb-derived states to the band frontiers in API-PbX_4 and PEA$_2$-PbX_4, the spin-orbit interaction lowers the energy of conduction-band minimum states (see Fig. S5). This energy reduction of Pb:p conduction-band states is well known in Pb- and Sn-containing HOP and LHOP systems [14,15,29,48] and attributed to the large mass of Pb atoms. Hence, SOC-related energy contributions are critical for correctly predicting the energetic ordering of states near the band extrema and, in particular, to *qualitatively* explain the relative energy position of organic π and π^* states. In Fig. 2 [as well as Figs. S4(a), S4(b), and S5(a) in the SM] we clearly show that once SOC is taken into account, the ion-resolved band ordering at the Γ-point conduction band minimum changes: The Pb:p states are lowered in energy relative to the API π^* states, which remain unaffected by the spin-orbit interaction. As a result, we observe Pb:p character for all **k** points throughout the BZ. In contrast, without the inclusion of SOC, a band inversion occurs at the Γ point and the conduction band minimum would be attributed to mostly API π^* states. Hence, if SOC is neglected, electronic-structure calculations could, depending on transition matrix element amplitude, incorrectly predict that excitations from the Γ-point band frontiers result in charge separation between perovskite and API layers. This behavior is different from what has been observed for 3D MAPbX_3 HOPs, for which ion projection of the band frontiers remain the same, with X+Pb and Pb attributed to the valence and conduction band frontiers, respectively [61], whether or not SOC is included. Finally, we note that the difference
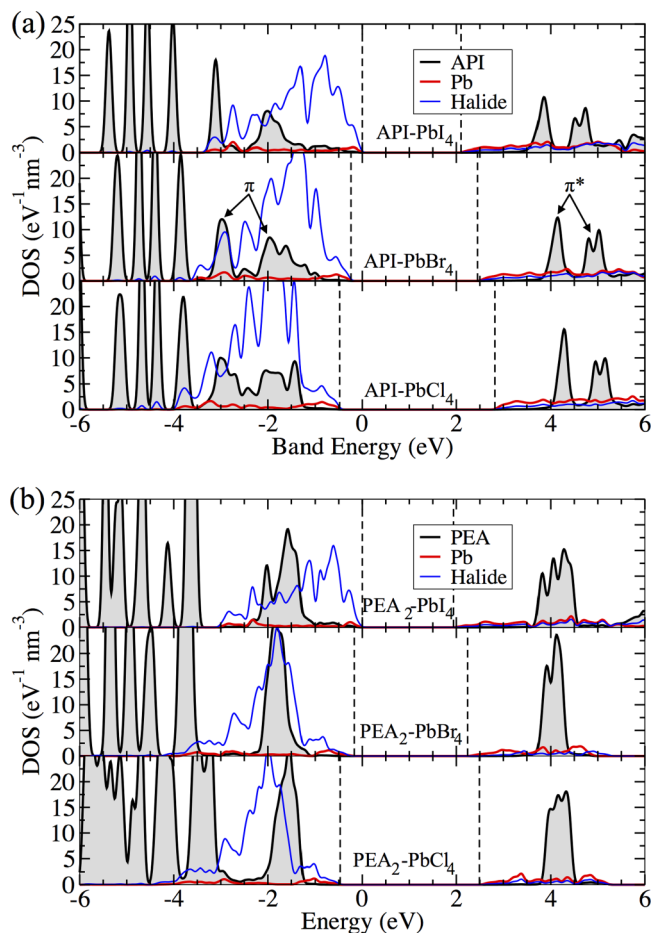
FIG. 3. The PBE+SOC+Δ_{HSE06} ion-projected DOS of (a) API-PbI$_4$, API-PbBr$_4$, and API-PbCl$_4$ and (b) PEA$_2$-PbI$_4$, PEA$_2$-PbBr$_4$, and PEA$_2$-PbCl$_4$. The energies of the Pb 5d states at -15.3 eV are used for alignment, and the valence band maxima of API-PbI$_4$ and PEA$_2$-PbI$_4$ are used as energy zero. Dashed lines mark the band extrema. Color coding: Pb (red), halide (blue), organic layer (shaded brown).

between HSE06+SOC and the PBE+SOC+Δ_{HSE06} approach is minimal, and PBE+SOC+Δ_{HSE06} calculations are a good basis for optical response calculations. To this end we show in detail in the SM that, for optical excitations energies below 5 eV, only small errors of under 0.5 eV are expected for spectral features.

The ion-resolved density of states (DOS) in Fig. 3 illustrates that in all six perovskite systems the valence- and conduction-band frontiers are attributed to halide and Pb states, respectively. For this analysis, we aligned the Pb:5d states at -15.3 eV across the different materials. Importantly, Fig. 3 shows a reduction of the valence-band maximum in energy with decreasing halide mass: The valence band maxima of API-PbX_4 shift from 0.0 to -0.24 and -0.48 eV for $X =$ I, Br, and Cl, respectively. The same trend of the valence band maximum located at 0.0, -0.17, and -0.47 eV occurs for the PEA$_2$-PbX_4 systems for $X =$ I, Br, and Cl, respectively. This decrease can be understood by examining standard atomic ionization energies of halide atoms, with I, Br, and Cl having ionization energies of 10.45, 11.81, and

12.96 eV (from the NIST Atomic Spectra Database Ionization Energies Form) [62]. Since the valence-band maximum of each perovskite material in this work is attributed to halide p states, our findings are commensurate with trends of these atomic ionization energies.

At the same time, this figure shows that organic π and π^* states are not affected by the changing halide mass and remain approximately aligned in both systems. The API π states appear as broad peaks at -2.00, -1.78, and -1.40 eV for I, Br, and Cl, respectively. This broadening is due to static molecular disorder and coupling between organic molecular states. The lowest energy π^* states appears as sharp peaks centered around 3.87, 4.10, and 4.30 eV for I, Br, and Cl, respectively. The resulting π-π^* gaps, defined as the energy differences of these peaks, are 5.87, 5.88, and 5.70 eV and show a width of about 0.5 eV from the broadening of the π^* state. The PEA$_2$-PbX_4 systems display a highest occupied π state peak spanning the range between -1.3 and -2.1 eV. A single lowest unoccupied π^* peak is located between 3.84 and 4.10 eV for all PEA$_2$-PbX_4 materials. This leads to π-π^* gaps of 5.39, 5.82, and 5.53 eV for I, Br, and Cl, respectively, with a width of about 1.0 eV. The variations in the π-π^* gaps in the PEA$_2$-PbX_4 systems are attributed to differences in the experimental x-ray atomic structures of the organic layers used in the unit cells of this study. As we chose to relax the API-PbX_4 structures [due to the similarities of the relaxed and experimental API-PbBr$_4$ structures and the lack of available experimental data for API-Pb(I, Cl)$_4$] the π-π^* gaps are uniform across the choice of halide. We note that quasiparticle corrections computed within HSE06+SOC also produce an energy-dependent band dilation, not reproduced by the scissor approach. This increases the π-π^* gaps of the API and PEA systems to about 6.1–6.3 eV, suggesting that π-π^* optical transitions will occur well in the UV photon energy range. The PBE+SOC+Δ_{HSE06} approximation captures the UV response of the intra-organic transitions, albeit at slightly lower energies compared to HSE06+SOC, and therefore provides a reasonable approximation for optical response calculations. It should be mentioned that, in reality, the absorption onset of such molecules is at lower energies due to large exchange energy contributions. For example, benzene in an alcohol solution has an absorption onset of about 4.8 eV [63]. However, this is still in the UV energy range.

Figure 3 also shows that, due to a lower cation charge of $+1$ on PEA compared to $+2$ in API, the ratio of organic to inorganic density of states is higher in the PEA$_2$-PbX_4 structures. This implies that, if organic-perovskite optical transitions are allowed, the PEA$_2$-PbX_4 systems have more possible charge-separation pathways under optical excitation. In examining the ion-resolved density of states of API-PbX_4, it can be seen that the optical response below the 5.7 eV π-π^* gap contains mostly transitions between perovskite-derived states. Only small contributions due to transitions from perovskite-to API-derived states are expected between the optical onset and 5.7 eV. This changes in the PEA$_2$-PbX_4 systems, where the PEA density of states amplitude in the valence and is about equal to or greater than the perovskite density of states at the PEA π-state energy. Consequently, the optical response could have a large contribution from perovskite to PEA transitions at lower energies than the π-π^* gap. This implies that if
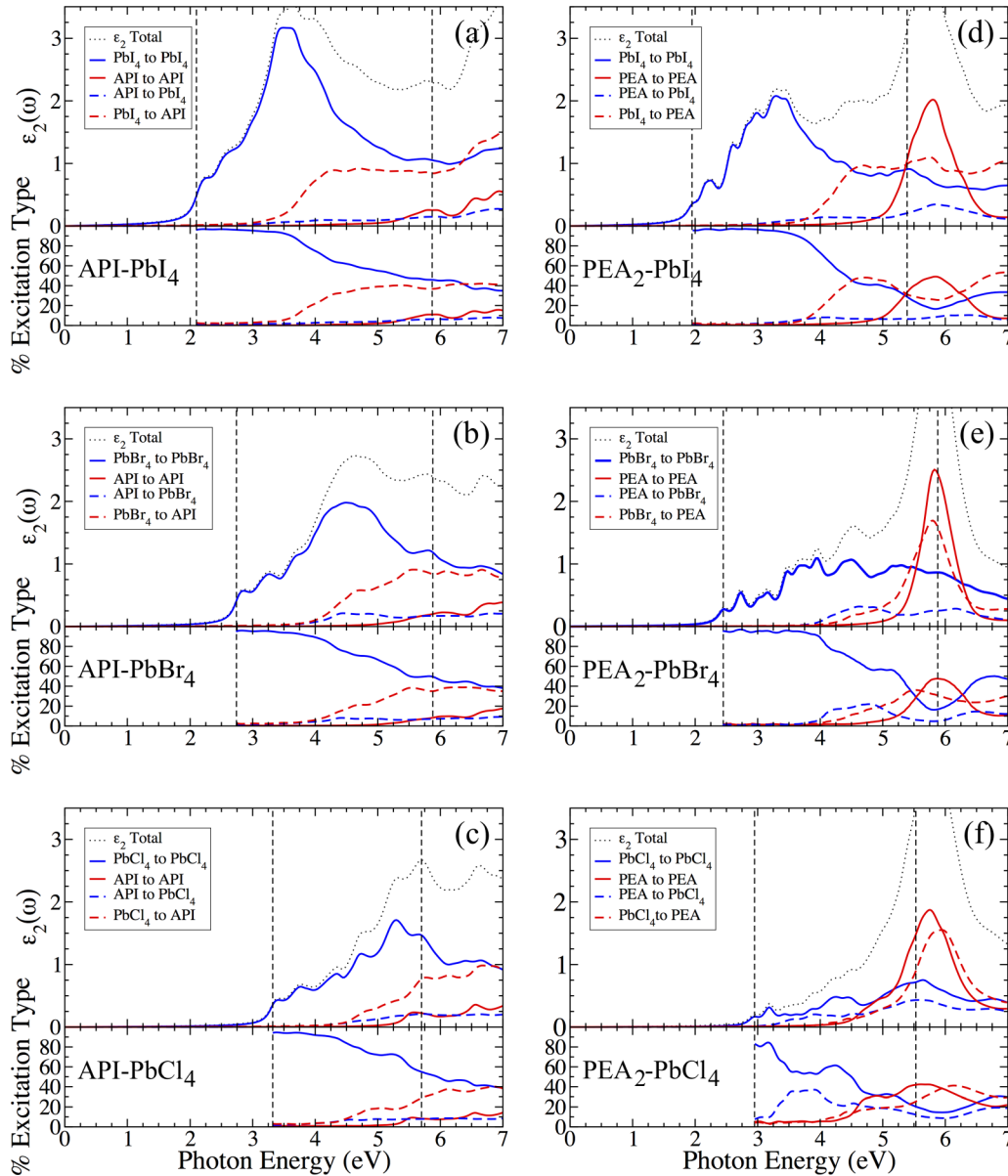
FIG. 4. The ion-resolved imaginary dielectric functions of (a) API-PbI$_4$, (b) API-PbBr$_4$, (c) API-PbCl$_4$, (d) PEA$_2$-PbI$_4$, (e) PEA$_2$-PbBr$_4$, and (f) PEA$_2$-PbCl$_4$. The color coding indicates the resolution of ε_2 along specific ion-to-ion transitions, which are (in valence ions → conduction ions notation) perovskite→perovskite (blue, solid), organic→organic (red, solid), organic→perovskite (blue, dashed), perovskite→organic (red, dashed), and all (black, dotted). The bottom panels show the percent that each type of transitions contributes to the total ε_2 as a function of photon energy.

transitions between perovskite and PEA are optically allowed, the PEA$_2$-PbX_4 systems have more possible charge separation states available.

Finally, in the context of achieving charge separation between organic and perovskite layers upon optical excitation, we find that PEA$_2$-PbCl$_4$ is a particularly promising candidate. The ion-resolved DOS in Fig. 3 shows a pronounced peak associated with the organic molecule that is centered near 1.5 eV below the valence-band maximum. Not only is this peak higher in energy than another peak at −2 eV that is attributed to Cl ions, but it also is of the same magnitude, as discussed above. This energetic positioning of states suggests the strong potential for partial charge separation, generating holes in the PEA$_2$ π state and electrons in the conduction-

band Pb:6p state. The actual probability of charge separation between layers, however, depends again on the dipole matrix elements for the corresponding optical transitions between these organic and perovskite states. This will be discussed next.

Optical response. The ion-projected dielectric function $\varepsilon_2(\omega)$ is illustrated in Fig. 4 for all considered materials. Here we distinguish between transitions among perovskite ions ("inorganic") and organic cations ("organic") by bundling them into the inorganic-inorganic, organic-organic, organic-inorganic and inorganic-organic subcategories. The first two correspond to intralayer transitions and the latter two to interlayer transitions. If the two sublayers were to act as separate optically active materials, the amplitude of interlayer

$\varepsilon_2(\omega)$ would be vanishing. In the case of intralayer optical excitation, these projections are finite.

By ion-resolving the imaginary dielectric function of API-PbX_4, we show that optical excitations below 4 eV are entirely dominated by intraperovskite transitions, whereas interlayer transitions contribute significantly to the optical response above 4 eV. As discussed above, this is because states in the vicinity of the gap are attributed entirely to perovskite states (Fig. 3). Absorption between API-derived states, with an onset around the π-π^* gap, contributes weakly to the overall optical response even in the UV energy range due to a low relative API-π density of states compared to the halide density of states in the valence band. Figure 4 also shows that transitions from PbX_4 to API states are responsible for a significant portion of the optical response in the UV energy range, and thus partial electron and hole separation occurs between the API and PbX_4 layers. However, this partial separation has little utility for optoelectronic applications requiring charge separation for visible light energy excitations.

The PEA$_2$-PbX_4 systems demonstrate a much stronger intraorganic optical response within the PEA layers, along with significant interlayer absorption in the UV energy range. As with API-PbX_4, the near-gap and visible energy range of the spectra is governed by intraperovskite optical response. Around the π-π^* gap, a large peak appears in the imaginary dielectric function which is attributed to the intra-PEA optical transitions and transitions from PbX_4 to PEA states. Transitions from PbX_4 to PEA states appear at higher energies at lower halide masses, corresponding to the increased VBM-π^* gap by the decrease in the valence band energy. In PEA$_2$-PbI$_4$, strong transitions are observed from PbI$_4$ to PEA states at lower energies than those between PEA states, leading to the same partial charge separating activity seen in API-PbX_4 above 4 eV. In PEA$_4$-PbBr$_4$, the contributions due to transitions from PbBr$_4$ to PEA and PEA to PbBr$_4$ are roughly equal in the 4 to 5 eV photon range, leading to a cancellation in partial charge separation character due to hybridization. PEA$_2$-PbCl$_4$ shows a change in behavior: The optical response between 3.5 and 4 eV largely arises from intraperovskite transitions and contributions from PEA to PbCl$_4$ states, partially separating holes to the PEA layer and electrons to the PbCl$_4$ layer. This behavior is due to the proximity of the PEA π states to the PbCl$_4$ attributed valence band maximum, leading to interlayer transitions closer to the absorption onset. However, overall, in PEA$_2$-PbX_4, where the organic optical activity is more significant compared to API-PbX_4, partial charge separation only occurs in the UV energy range.

In all three LHOP API-PbX_4 compounds, excitonic effects are expected to be stronger compared to their 3D HOP MAPbX_3 counterparts owing to quantum and dielectric confinement effects [30]. This increased binding energy was first explained by the works of Rytova and Keldysh, who separately established the theory of quantum confinement of charge carriers and the Coulomb interaction in low dimensional systems [64,65]. This was further explored in layered semiconductors by Hanamura and layered perovskites by Ishihara and Koutselas [66–69]. In 3D HOPs such as MAPbI$_3$, MAPbBr$_3$, and MAPbCl$_3$, the high-frequency dielectric constants ε_∞ are about 4–7 [48,70–72]. MAPbX_4

also has highly dispersive band frontiers, leading to a low reduced electron-hole mass of about $0.1 m_0$ [73]. Using a simple Wannier-Mott model, the exciton binding energy is in the range of 25 to 85 meV. As determined in experiments and predicted by theory, the low-frequency dielectric constants are also large ($\varepsilon_s > 20$), which enhances the screening of the electron-hole Coulomb potential [29,73–76]. Given the API-PbBr$_4$ electronic structure determined in this work, the high-frequency dielectric constant is determined to be 3.94 by density-functional perturbation theory (DFPT) and the reduced electron-hole mass at the band frontiers is approximately $0.610 m_0$, based on an averaged parabolic fit to the dispersive, in-plane, $Y \to G$ and $Y \to A$ directions. This leads to a Wannier-Mott binding energy of 525 meV, which is an order of magnitude higher compared to the 3D counterparts. The lower high-frequency dielectric constants predicted by DFPT range from 3.47 to 4.76 for the LHOP systems (see Table S2) and originate from the alternating low and high values of ε_∞ between layers averaged over the unit cell volume [77]. This leads to an average dielectric constant that is lower than those typically measured and calculated for 3D HOPs [29,30].

The excitation energies of lone API molecules in air are calculated in the Gaussian suite [78] to determine if the organic optical response will contribute a significant portion of the optical response near the perovskite absorption edge. The HSE06, B3LYP, and CAM-B3LYP functionals are used to calculate the gaps between the highest occupied molecular orbital and lowest unoccupied molecular orbital (HOMO-LUMO gaps) of 5.60, 5.84, and 8.05 eV respectively in the singlet-relaxed geometry. The HSE06 and B3LYP results agree very well with the π-π^* gap found in API-PbX_4 at the PBE+SOC+Δ_{HSE06} level of theory. Excitation energies are calculated using time-dependent DFT and are found to be 5.42, 5.23, and 5.75 eV within the HSE06, B3LYP, and CAM-B3LYP functionals, respectively. These results suggest that the excitonic absorption onset of the API spacer will not occur near the perovskite excitonic absorption edge.

Strong excitonic effects and, hence, large exciton binding energies are predicted for the API-PbX_4 materials from first principles, with values comparable to available experimental data for LHOP systems. For API-PbX_4, we show in Fig. 5 that excitonic effects significantly influence the optical-absorption spectra. The gradual absorption onset observed in the single-particle dielectric function becomes a pronounced excitonic peak, redshifted to lower energy, that is associated with the lowest-energy electron-hole bound state. In addition, there is also a significant redshift of broad high-energy peak structures between 3.5 and 4.5 eV, resulting in strongly increased absorption at lower energies. In our calculations, the energy difference of the onsets of single-particle and BSE spectrum correspond to the binding energy of the lowest electron-hole pair. The high computational cost of the BSE calculations in this work, due to large unit cells and inclusion of spin-orbit coupling, does not allow a dense enough multiple **k**-point sampling [79] to provide fully converged results for this quantity. Given the choice of **k**-point mesh, we estimate that our numbers are within 100 meV of the converged result (see SM Fig. S6). From our data we extract $\approx$357 meV (see Fig. 5) for the exciton-binding energy of API-PbI$_4$, which is the smallest
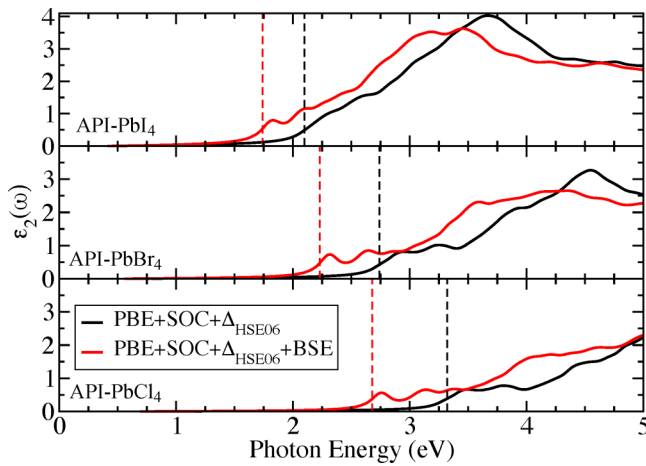
FIG. 5. Imaginary part of the dielectric function of API-PbI$_4$ (top), API-PbBr$_4$ (middle), and API-PbCl$_4$ (bottom) with (red lines) and without (black lines) excitonic effects. The PBE+SOC Kohn-Sham energies and states are used as input to the BSE and the single-particle band gap is shifted to the HSE06+SOC value. That band gap and the lowest excitation from the BSE are marked by vertical black and red dashed lines, respectively.

value for the three API-PbX_4 compounds studied in this work. API-PbBr$_4$ shows a stronger exciton binding energy due to the lower dielectric constant compared to API-PbI$_4$, and consequently a stronger redshift of the onset by ≈ 505 meV. Finally, the strongest excitonic redshift in the optical spectrum of ≈ 638 meV is predicted for API-PbCl$_4$, with the lowest high-frequency dielectric constant. High-frequency dielectric constants are slightly overestimated as they are calculated at the PBE+SOC level of theory. However, from test calculations we estimate that increasing the band gap to the experimental value would decrease the dielectric constant by less than 15%. Since we do not have accurate band gap data to compare with for the API-PbX_4 materials, we use the PBE+SOC high-frequency dielectric constant as a good approximation.

The predicted exciton binding energies and relative positions of spectral peaks are in good agreement with available experimental data of layered perovskite systems [47]. Wang *et al.* measured exciton binding energies of 218 meV in hexadecammonium-lead bromide (HA)$_2$PbBr$_4$ [80], Blancon *et al.* measured binding energies of 380, 270, and 220 meV in $n = 1$, $n = 2$, and $n > 2$-layered (BA)$_2$(MA)$_{n1}$Pb$_n$I$_{3n+1}$ [39], and Ishihara *et al.* calculated a binding energy of 320 meV in $n = 1$ layered PbI$_4$ octahedra with no organic spacer [67]. As a model function relying on a single, material-averaged dielectric constant is used to compute the screened Coulomb interaction between electrons and holes, we do not account for the local field effects arising from the high spatial variability of the dielectric constant in LHOPs [29,30]. More precise techniques such as including the full inverse dielectric tensor $\varepsilon_{G,G'}(q)^{-1}$ or semiclassical and semiempirical methods that describe dielectric constant fluctuations can be used for a higher degree of accuracy [29,81–83]. These high binding energies are also potentially detrimental to solar cell applications which rely on splitting of electron-hole pairs. Investigations by Smith *et al.* have shown that the introduction of

halogens by I$_2$ intercalation into the organic layer strongly reduces binding energy and the dielectric confinement of the layered perovskite systems [84], potentially lowering the exciton binding energy of LHOPs which is preferable for photo-voltaic application.

III. CONCLUSIONS AND FUTURE DIRECTION

This computational study predicts that the optical response of single-layered lead-halide perovskites with single-π-conjugated organic layers API and PEA$_2$ is dominated by intraperovskite optical excitations in the visible energy range. A partial charge separation between the organic perovskite states can only be achieved at UV energies. Given these results, we conclude that single-layered PbX_4 LHOP systems with π-organic cation spacing layers composed of moieties with single aromatic rings act as one optically active perovskite material. Transitions involving both layers only occur at UV photon energies. Importantly, the lack of π and π^* states near the band extrema causes transitions in the visible energy range to be contained within the perovskite layer, meaning all electron-hole generation for optoelectronic applications in this energy range will be localized to the PbX_4 octahedral layers. At UV energies, significant electronic delocalization and charge separation is allowed; however, the corresponding excitation energies are close to or above the ionization energy of perovskite systems.

The natural followup question is, how can charge separation be further achieved in layered hybrid perovskite systems? The first item that must be addressed is the π-π^* gap of the conjugated groups. As discussed above, the absorption onset of single aromatic ring moieties occurs well below the HOMO-LUMO gap due to large exciton binding energies on the order of electron volts [85]. Benzene, with an optical onset of 4.8 eV experimentally and between 4.7 and 6.9 eV theoretically by PBE0+BSE and GW+BSE calculations [63,86], has a predicted HOMO-LUMO gap in solution of between 4.5 and 6 eV [87]. Likewise, imidazole has a range of predicted excitation energies between 5.61 and 6.96 eV [86]. Thus, the interplay between the HOMO-LUMO gap and the optical gap should be carefully considered in further engineering of layered perovskites for interlayer charge separation application. Ideally, the HOMO-LUMO gap can be lowered by adding more conjugated groups such as aromatic rings to the system. For example, layered perovskites with naphthalene groups have been investigated experimentally and have shown signs of exciton energy transfer between perovskite and organic layers [41,42]. Secondly, the orbital overlap between the layers must be improved to increase the amplitude of the inter-layer transition dipole matrix elements. Larger overlap could be achieved by including heavier elements, such as chlorine, in the organic layer, which has been recently explored experimentally [36,38,88]. Our future studies of such compounds will include organic-PbX_4 ion-projected band structures and densities of states to map the effects of decreased HOMO-LUMO organic gap and organic halogenation.

Currently, $n = 1$ LHOPs with single conjugated rings face challenges as effective solar cell materials but show promise in a wide range of optoelectronic applications. Quantum

confinement of the perovskite layer increases the gap relative to the 3D HOPs and thus reduces the absorption range of the material in the visible optical spectrum. LHOPs with $n > 1$ help to decrease the gap [32], but at the cost of reducing the density of states of, and degree of optical coupling to, the organic lattice. Secondly, minimal π-stacking is observed in these systems, leading to highly localized electron and hole states in the organic layer. This in turn results in a high effective mass, low mobility in the form of incoherent hopping, and large binding energies of electron-hole pairs. Improving π-stacking of the organic conjugated layer in LHOPs is a promising future research direction to achieve improvements [89]. Recent investigations have also shown that interfacing 2D LHOPs with 3D HOPs can lead to increased photovoltaic efficiency in Sn-based systems, opening the intriguing question of whether this can be done with Pb-based systems as well [90]. Besides applications as solar cells, $n = 1$ layered perovskites have shown promise as light emitters [91]. Resonant coupling between the organic and perovskite layered of $n = 1$ systems opens the possibility of engineering the emission wavelength and intensity as a function of LHOP stoichiometry [42,92].

It is important to note that everything studied in this manuscript is related purely to absorption in the singlet spin state. Thus, nothing is said about relaxation in the excited state or emission in the explored LHOP systems. Both triplet and singlet energy levels and their post-optical absorption dynamics are fundamental to understanding how organic compounds behave in the excited state. The interplay between perovskite band energies and the organic singlet and triplet states must be understood to determine excited state charge transport, ion dynamics, and recombination in LHOPs with conjugated organic layers. The combination of methods in this work for determining optical absorption properties and methods such as time-dependent density functional theory and molecular dynamics can be used to predict and disentangle the full optical excitation and relaxation process of conjugated LHOP materials.

APPENDIX: COMPUTATIONAL DETAILS

DFT calculations, using the projector-augmented wave method, are performed with the Vienna *Ab Initio* Simulation Package (VASP) [93–96]. The generalized-gradient approximation of Perdew, Burke, and Ernzerhof (PBE) [97] is used to describe exchange and correlation (XC). Kohn-Sham wave functions are expanded into a plane-wave basis with an energy cutoff of 500 eV and the Brillouin zone (BZ) is sampled using a Γ-centered $4 \times 4 \times 2$ **k**-point mesh. With this setup, total energies of the API-PbX_4 structures are converged to within 5 meV per formula unit. Equilibrium positions of all atoms, cell volumes, and unit cell parameters are optimized by minimizing the external pressure and Hellman-Feynman forces to below a threshold of 10^{-2} eV/Å using the PBEsol XC functional [98] and an increased plane-wave cutoff of 900 eV. The use of PBEsol is based on previous studies where lattice parameters of hybrid perovskite materials are predicted to high accuracy [59]. The symmetries of the experimentally determined unit cell are preserved in the first-principles atomic position and cell geometry relaxation. Band structures, ion-resolved densities of states (DOS), and ion-resolved optical-absorption spectra are calculated, taking spin-orbit coupling (SOC) into account [99]. The high-frequency dielectric constant ε_∞ is calculated using density functional perturbation theory on a $5 \times 5 \times 2$ Γ-centered **k**-point mesh for API-PbX_4 (see Supplemental Material Fig. S1). Band gaps are determined using the Heyd-Scuseria-Ernzerhof (HSE06) hybrid XC functional [100] with a fraction of $\alpha = 0.25$ exact exchange. Due to the high computational cost of including SOC in hybrid functional calculations, these are performed using a $2 \times 2 \times 2$ Γ-centered **k**-point mesh.

Linear optical response, described by the components of the complex frequency-dependent dielectric tensor $\varepsilon^{\alpha\beta}(\omega)$, where α and β are Cartesian coordinates, is computed using the Ehrenreich-Cohen formula [77,101]:

$$\varepsilon_2^{\alpha\beta}(\omega) = \frac{8\pi^2 e^2}{\Omega} \sum_{cvk} \frac{\langle \phi_{ck}|\hat{p}_\alpha|\phi_{vk}\rangle \langle \phi_{vk}|\hat{p}_\beta|\phi_{ck}\rangle^*}{(\epsilon_{ck} - \epsilon_{vk})^2}$$
$$\times \delta(\epsilon_{ck} - \epsilon_{vk} - \hbar\omega). \qquad \text{(A1)}$$

Here, ϵ_{ck} and ϵ_{vk} are the conduction and valence band energies of the single-particle states at electronic wave vector **k**, along with their respective Kohn-Sham wave functions ϕ_{ck} and ϕ_{vk}. $\hat{p}_\beta$ is the Cartesian component of the momentum operator and Ω is the volume of the unit cell. We use PBE+SOC Kohn-Sham energies and wave functions and a scissor shift to adjust the energies of the conduction bands to the HSE06+SOC band gap (referred to as PBE+SOC+Δ_{HSE06}). The transition-matrix elements in Eq. (A1) are computed using the VASP code [77].

We also compute the ion- and angular-momentum resolved optical response by weighting the transition-matrix element for a given transition using the projection p_{lmnk}^N of the wave function ϕ_{nk} on a spherical harmonic Y_{lm} for a given ion N, with m and l being the magnetic and orbital quantum number,

respectively [102]. The sum of p_{lmnk}^N over all N, l, and m equals 1 for each wave function ϕ_{nk}. This turns Eq. (A1) into

$$\varepsilon_2^{\alpha\beta}(\omega) = \frac{8\pi^2 e^2}{\Omega} \sum_{cvk} \left(\sum_{N,l,m} p_{lmnk}^N \right)$$
$$\times \frac{\langle\phi_{ck}|\hat{p}_\alpha|\phi_{vk}\rangle\langle\phi_{vk}|\hat{p}_\beta|\phi_{ck}\rangle^*}{(\epsilon_{ck} - \epsilon_{vk})^2} \delta(\epsilon_{ck} - \epsilon_{vk} - \hbar\omega). \quad \text{(A2)}$$

Restricting the sum in parentheses to certain ions, angular-momentum components, or bands (e.g., n being v or c when resolving valence or conduction states), allows us to compute ion- and angular-momentum resolved optical response.

In addition, we study excitonic effects on the dielectric functions of API-PbX_4 from the solution of the Bethe-Salpeter equation (BSE) [79,103,104] for the optical polarization function. The large computational cost of this approach requires us to restrict these calculations to a $4 \times 4 \times 2$ **k**-point grid. A small random shift of this grid lifts degeneracies and, on the DFT level, allows us to reproduce dielectric functions calculated on a well-converged Γ-centered $8 \times 8 \times 2$ **k**-point grid (see Supplemental Material, Fig. S6). The absorption edges from shifted and well-converged Γ-centered **k**-point grids disagree by about 100 meV. Converging exciton-binding energies, defined as the difference between the lowest optical and the lowest single-particle excitation energies, to high accuracy requires much denser **k**-point sampling near the band extrema [79], which is beyond the scope of this study. Hence, estimates for exciton-binding energies reported here have error bars of about 100 meV.

The screened electron-hole Coulomb interaction W in the BSE kernel is calculated using the model dielectric function proposed by Cappellini *et al.* [105]. The dielectric constant used in the model dielectric function is the average of the diagonal components of the high-frequency dielectric tensor $\varepsilon_\infty^{\alpha\beta}$ calculated by density functional perturbation theory

(DFPT) (see Supplemental Material Table S1), representing the average dielectric response of the layered material. It has been extensively shown that the organic and perovskite layers of LHOPs have spatially resolved dielectric constants of ≈ 2.5 and 5 respectively [29,30], and thus this work will use the spatially averaged dielectric constant determined by DFPT as an approximate value [77]. Other methods are available in the literature to handle this spatial variability of the dielectric constant [29,81,82]. In this work, the BSE is solved as an eigenvalue problem in the Bloch basis [79,104] of the excitonic Hamiltonian, and using the Tamm-Dancoff approximation:

$$H_{cvk}^{c'v'k'} = (\epsilon_{ck} - \epsilon_{vk})\delta(cc')\delta(vv')\delta(kk') - W_{cvk}^{c'v'k'} + 2\bar{V}_{cvk}^{c'v'k'}. \quad \text{(A3)}$$

Here, band energies ϵ_{ck} and ϵ_{vk} from the PBE+SOC+Δ_{HSE06} level of theory are used. Noninteracting electron-hole pairs with energies up to 5 eV (applied to the PBE+SOC band structure) are used to compute the excitonic Hamiltonian. These include, in (nv, nc, nk) format: API-PbI4 (112,48,32), API-PbBr4 (110,40,32), and API-PbCl4 (104,32,32). Matrix elements $W_{cvk}^{c'v'k'}$ of the attractive electron-hole Coulomb potential and $\bar{V}_{cvk}^{c'v'k'}$ of the local repulsive Coulomb potential are computed using spin-polarized Kohn-Sham wave functions. The eigenvalues E^λ of $H_{cvk}^{c'v'k'}$ describe optical λth excitation energies, with excitonic states A_{cvk}^λ being the eigenvectors, and they can be determined by solving the eigenvalue equation for $H_{cvk}^{c'v'k'}$. Dielectric functions, including excitonic effects, are calculated from the excitonic Hamiltonian in Eq. (A3) using a time-propagation technique [106,107]. The rigid band gap shift is added to the diagonal of the excitonic Hamiltonian, increasing the energy window of the excitonic Hamiltonian from 5 eV to 5+Δ_{HSE06} eV. For the above-mentioned energy window of 5 eV, 5594 time steps of 0.0022 per eV are required. The lowest excitation energies are found by applying a conjugate-gradient scheme to iteratively compute the lowest eigenvalues. All these calculations are carried out using the BSE implementation discussed in Refs. [79,108].

[1] A. Mei, X. Li, L. Liu, Z. Ku, T. Liu, Y. Rong, M. Xu, M. Hu, J. Chen, Y. Yang, M. Grätzel, and H. Han, Science **345**, 295 (2014).

[2] M. M. Lee, J. Teuscher, T. Miyasaka, T. N. Murakami, and H. J. Snaith, Science **338**, 643 (2012).

[3] R. Sheng, A. Ho-Baillie, S. Huang, S. Chen, X. Wen, X. Hao, and M. A. Green, J. Phys. Chem. C **119**, 3545 (2015).

[4] A. Kojima, K. Teshima, Y. Shirai, and T. Miyasaka, J. Am. Chem. Soc. **131**, 6050 (2009).

[5] J.-H. Im, C.-R. Lee, J.-W. Lee, S.-W. Park, and N.-G. Park, Nanoscale **3**, 4088 (2011).

[6] W. S. Yang, J. H. Noh, N. J. Jeon, Y. C. Kim, S. Ryu, J. Seo, and S. I. Seok, Science **348**, 1234 (2015).

[7] M. A. Green, Y. Hishikawa, E. D. Dunlop, D. H. Levi, J. Hohl-Ebinger, and A. W. Ho-Baillie, Prog. Photovoltaics **26**, 3 (2017).

[8] J. Luo, J.-H. Im, M. T. Mayer, M. Schreier, M. K. Nazeeruddin, N.-G. Park, S. D. Tilley, H. J. Fan, and M. Grätzel, Science **345**, 1593 (2014).

[9] S. Yakunin, M. Sytnyk, D. Kriegner, S. Shrestha, M. Richter, G. J. Matt, H. Azimi, C. J. Brabec, J. Stangl, M. V. Kovalenko, and W. Heiss, Nat. Photonics **9**, 444 (2015).

[10] H. Wei, Y. Fang, P. Mulligan, W. Chuirazzi, H.-H. Fang, C. Wang, B. R. Ecker, Y. Gao, M. A. Loi, L. Cao, and J. Huang, Nat. Photonics **10**, 333 (2016).

[11] S. Yakunin, L. Protesescu, F. Krieg, M. I. Bodnarchuk, G. Nedelcu, M. Humer, G. De Luca, M. Fiebig, W. Heiss, and M. V. Kovalenko, Nat. Commun. **6**, 8056 (2015).

[12] Y. He, L. Matei, H. J. Jung, K. M. McCall, M. Chen, C. C. Stoumpos, Z. Liu, J. A. Peters, D. Y. Chung, B. W. Wessels, M. R. Wasielewski, V. P. Dravid, A. Burger, and M. G. Kanatzidis, Nat. Commun. **9**, 1609 (2018).

[13] Z.-K. Tan, R. S. Moghaddam, M. L. Lai, P. Docampo, R. Higler, F. Deschler, M. Price, A. Sadhanala, L. M. Pazos, D. Credgington, F. Hanusch, T. Bein, H. J. Snaith, and R. H. Friend, Nat. Nanotechnol. **9**, 687 (2014).

[14] J. Even, L. Pedesseau, J.-M. Jancu, and C. Katan, J. Phys. Chem. Lett. **4**, 2999 (2013).

[15] M. Kepenekian and J. Even, J. Phys. Chem. Lett. **8**, 3362 (2017).

[16] X. Hu, X. Zhang, L. Liang, J. Bao, S. Li, W. Yang, and Y. Xie, Adv. Funct. Mater. **24**, 7373 (2014).

[17] M. Espinosa, Nieves, L. Serrano-Lujan, A. Urbina, and F. C. Krebs, Sol. Energ. Mater. Sol. Cells **137**, 303 (2015).

[18] B. Hailegnaw, S. Kirmayer, E. Edri, G. Hodes, and D. Cahen, J. Phys. Chem. Lett. **6**, 1543 (2015).

[19] J. Gong, S. B. Darling, and F. You, Energy Environ. Sci. **8**, 1953 (2015).

[20] A. Babayigit, A. Ethirajan, M. Muller, and B. Conings, Nat. Mater. **15**, 247 (2016).

[21] P.-Y. Chen, J. Qi, M. T. Klug, X. Dang, P. T. Hammond, and A. M. Belcher, Energy Environ. Sci. **7**, 3659 (2014).

[22] L. Li, G. Qi, C. Yuan, Y. Sun, X. Lei, H. Xu, and Y. Wang, Energy Environ. Sci. **8**, 1616 (2015).

[23] W. Huang, J. S. Manser, P. V. Kamat, and S. Ptasinska, Chem. Mater. **28**, 303 (2016).

[24] W. Nie, J.-C. Blancon, A. J. Neukirch, K. Appavoo, H. Tsai, M. Chhowalla, M. A. Alam, M. Y. Sfeir, C. Katan, J. Even, S. Tretiak, J. J. Crochet, G. Gupta, and A. D. Mohite, Nat. Commun. **7**, 11574 (2016).

[25] A. J. Neukirch, W. Nie, J.-C. Blancon, K. Appavoo, H. Tsai, M. Y. Sfeir, C. Katan, L. Pedesseau, J. Even, J. J. Crochet, G. Gupta, A. D. Mohite, and S. Tretiak, Nano Lett. **16**, 3809 (2016).

[26] E. L. Lucas and E. R. Jarvo, Acc. Chem. Res. **51**, 567 (2018).

[27] J. Zhou, Y. Chu, and J. Huang, ACS Appl. Mater. Interfaces **8**, 25660 (2016).

[28] J. Even, L. Pedesseau, and C. Katan, Chem. Phys. Chem. **15**, 3733 (2014).

[29] L. Pedesseau, D. Sapori, B. Traore, R. Robles, H.-H. Fang, M. A. Loi, H. Tsai, W. Nie, J.-C. Blancon, A. Neukirch, S. Tretiak, A. D. Mohite, C. Katan, J. Even, and M. Kepenekian, ACS Nano **10**, 9776 (2016).

[30] B. Traore, L. Pedesseau, L. Assam, X. Che, J.-C. Blancon, H. Tsai, W. Nie, C. C. Stoumpos, M. G. Kanatzidis, S. Tretiak, A. D. Mohite, J. Even, M. Kepenekian, and C. Katan, ACS Nano **12**, 3321 (2018).

[31] J. Even, L. Pedesseau, J. Jancu, and C. Katan, Phys. Status Solidi R **8**, 31 (2014).

[32] H. Tsai, W. Nie, J.-C. Blancon, C. C. Stoumpos, R. Asadpour, B. Harutyunyan, A. J. Neukirch, R. Verduzco, J. J. Crochet, S. Tretiak, L. Pedesseau, J. Even, M. A. Alam, G. Gupta, J. Lou, P. M. Ajayan, M. J. Bedzyk, M. G. Kanatzidis, and A. D. Mohite, Nature (London) **536**, 312 (2016).

[33] M. D. Smith and H. I. Karunadasa, Acc. Chem. Res. **51**, 619 (2018).

[34] N. Kawano, M. Koshimizu, Y. Sun, N. Yahaba, Y. Fujimoto, T. Yanagida, and K. Asai, J. Phys. Chem. C **118**, 9101 (2014).

[35] S. N. Ruddlesden and P. Popper, Acta. Crystallogr. **11**, 54 (1958).

[36] G. Papavassiliou, Prog. Solid State Chem. **25**, 125 (1997).

[37] D. B. Mitzi, in *Progress in Inorganic Chemistry* (Wiley-Blackwell, New York, 2007), pp. 1–121.

[38] N. Mercier, N. Louvain, and W. Bi, Cryst. Eng. Commun. **11**, 720 (2009).

[39] J.-C. Blancon, H. Tsai, W. Nie, C. C. Stoumpos, L. Pedesseau, C. Katan, M. Kepenekian, C. M. M. Soe, K. Appavoo, M. Y.

Sfeir, S. Tretiak, P. M. Ajayan, M. G. Kanatzidis, J. Even, J. J. Crochet, and A. D. Mohite, Science **355**, 1288 (2017).

[40] M. Braun, W. Tuffentsammer, H. Wachtel, and H. Wolf, Chem. Phys. Lett. **307**, 373 (1999).

[41] M. Era, K. Maeda, and T. Tsutsui, Chem. Phys. Lett. **296**, 417 (1998).

[42] K. Ema, M. Inomata, Y. Kato, H. Kunugita, and M. Era, Phys. Rev. Lett. **100**, 257401 (2008).

[43] B. A. Gregg, J. Phys. Chem. B **107**, 4688 (2003).

[44] R. H. Friend, R. W. Gymer, A. B. Holmes, J. H. Burroughes, R. N. Marks, C. Taliani, D. D. C. Bradley, D. A. D. Santos, J. L. Brédas, M. Lögdlund, and W. R. Salaneck, Nature (London) **397**, 121 (1999).

[45] L. Rothberg, M. Yan, F. Papadimitrakopoulos, M. Galvin, E. Kwock, and T. Miller, Synth. Met. **80**, 41 (1996).

[46] N. C. Greenham, X. Peng, and A. P. Alivisatos, Phys. Rev. B **54**, 17628 (1996).

[47] Y. Y. Li, C. K. Lin, G. L. Zheng, Z. Y. Cheng, H. You, W. D. Wang, and J. Lin, Chem. Mater. **18**, 3463 (2006).

[48] P. Umari, E. Mosconi, and F. De Angelis, Sci. Rep. **4**, 4467 (2014).

[49] J. Yin, H. Li, D. Cortecchia, C. Soci, and J.-L. Brédas, ACS Energy Lett. **2**, 417 (2017).

[50] D. Cortecchia, J. Yin, A. Bruno, S.-Z. A. Lo, G. G. Gurzadyan, S. Mhaisalkar, J.-L. Bredas, and C. Soci, J. Mater. Chem. C **5**, 2771 (2017).

[51] M. D. Smith, A. Jaffe, E. R. Dohner, A. M. Lindenberg, and H. I. Karunadasa, Chem. Sci. **8**, 4497 (2017).

[52] L. Mao, Y. Wu, C. C. Stoumpos, B. Traore, C. Katan, J. Even, M. R. Wasielewski, and M. G. Kanatzidis, J. Am. Chem. Soc. **139**, 11956 (2017).

[53] K.-z. Du, Q. Tu, X. Zhang, Q. Han, J. Liu, S. Zauscher, and D. B. Mitzi, Inorg. Chem. **56**, 9291 (2017).

[54] M. S. Hybertsen and S. G. Louie, Phys. Rev. B **34**, 5390 (1986).

[55] D. G. Billing, Acta Crystallogr. E **58**, m669 (2002).

[56] K. Shibuya, M. Koshimizu, F. Nishikido, H. Saito, and S. Kishimoto, Acta Crystallogr. E **65**, m1323 (2009).

[57] D. B. Mitzi, J. Solid State Chem. **145**, 694 (1999).

[58] See Supplemental Material at http://link.aps.org/supplemental/10.1103/PhysRevMaterials.2.105406 for further computational details and supplemental results related to this work, including calculation parameter convergence for the Bethe-Salpeter Equation, ion-resolved band structures for all materials, and comparisons to PBE+SOC+HSE06 spectra.

[59] F. Brivio, J. M. Frost, J. M. Skelton, A. J. Jackson, O. J. Weber, M. T. Weller, A. R. Goñi, A. M. A. Leguy, P. R. F. Barnes, and A. Walsh, Phys. Rev. B **92**, 144308 (2015).

[60] A. Fraccarollo, V. Cantatore, G. Boschetto, L. Marchese, and M. Cossi, J. Chem. Phys. **144**, 164701 (2016).

[61] B. Joseph, B. Tonio, E. D. A., H. Gary, K. Leeor, L. Yueh-Lin, L. Igor, M. S. R., M. Yitzhak, M. J. S., M. D. B., P. Yaron, R. A. M., R. Ilan, R. Boris, S. Oscar, S. Vladan, T. M. F., Z. David, K. Antoine, G. David, and C. David, Adv. Mater. **27**, 5102 (2015).

[62] W. Martin, A. Musgrove, J. Kotochigova, and J. Sansonetti, Technical Report, National Institute of Standards and Technology, Gaithersburg, MD, 2013, Ground Levels and Ionization Energies for the Neutral Atoms.

[63] T. Inagaki, J. Chem. Phys. **57**, 2526 (1972).

[64] N. S. Rytova, Moscow Univ. Phys. Bull. **22**, 18 (1967).

[65] L. V. Keldysh, JEPT Lett. **29**, 658 (1979).

[66] E. Hanamura, Phys. Rev. B **38**, 1228 (1988).

[67] T. Ishihara, J. Takahashi, and T. Goto, Phys. Rev. B **42**, 11099 (1990).

[68] T. Ishihara, J. Takahashi, and T. Goto, Solid State Commun. **69**, 933 (1989).

[69] I. B. Koutselas, L. Ducasse, and G. C. Papavassiliou, J. Phys.: Condens. Matter **8**, 1217 (1996).

[70] M. A. Pérez-Osorio, R. L. Milot, M. R. Filip, J. B. Patel, L. M. Herz, M. B. Johnston, and F. Giustino, J. Phys. Chem. C **119**, 25703 (2015).

[71] M. Sendner, P. Nayak, D. Egger, S. Beck, C. Muller, B. Epding, W. Kowalsky, L. Kronik, H. J. Snaith, A. Pucci, and R. Lovrincic, Mater. Horiz. **3**, 613 (2016).

[72] M. Bokdam, T. Sander, A. Stroppa, S. Picozzi, D. D. Sarma, C. Franchini, and G. Kresse, Sci. Rep. **6**, 28618EP (2016).

[73] K. Galkowski, A. Mitioglu, A. Miyata, P. Plochocka, O. Portugall, G. E. Eperon, J. T.-W. Wang, T. Stergiopoulos, S. D. Stranks, H. J. Snaith, and R. J. Nicholas, Energy Environ. Sci. **9**, 962 (2016).

[74] J. Even, L. Pedesseau, and C. Katan, J. Phys. Chem. C **118**, 11566 (2014).

[75] A. Miyata, A. Mitioglu, P. Plochocka, O. Portugall, J. T.-W. Wang, S. D. Stranks, H. J. Snaith, and R. J. Nicholas, Nat. Phys. **11**, 582 (2015).

[76] T. Ishihara, J. Lumin. **60-61**, 269 (1994).

[77] M. Gajdoš, K. Hummer, G. Kresse, J. Furthmüller, and F. Bechstedt, Phys. Rev. B **73**, 045112 (2006).

[78] M. J. Frisch, G. W. Trucks, H. B. Schlegel, G. E. Scuseria, M. A. Robb, J. R. Cheeseman, G. Scalmani, V. Barone, G. A. Petersson, H. Nakatsuji, X. Li, M. Caricato, A. V. Marenich, J. Bloino, B. G. Janesko, R. Gomperts, B. Mennucci, H. P. Hratchian, J. V. Ortiz, A. F. Izmaylov *et al.* Gaussian 16 Revision B.01, 2016, Gaussian Inc., Wallingford, CT.

[79] F. Fuchs, C. Rödl, A. Schleife, and F. Bechstedt, Phys. Rev. B **78**, 085103 (2008).

[80] Q. Wang, X.-D. Liu, Y.-H. Qiu, K. Chen, L. Zhou, and Q.-Q. Wang, AIP Adv. **8**, 025108 (2018).

[81] E. A. Muljarov, S. G. Tikhodeev, N. A. Gippius, and T. Ishihara, Phys. Rev. B **51**, 14370 (1995).

[82] S.-L. Chuang, S. Schmitt-Rink, D. A. B. Miller, and D. S. Chemla, Phys. Rev. B **43**, 1500 (1991).

[83] J. C. Blancon, A. V. Stier, H. Tsai, W. Nie, C. C. Stoumpos, B. Traoré, L. Pedesseau, M. Kepenekian, F. Katsutani, G. T. Noe, J. Kono, S. Tretiak, S. A. Crooker, C. Katan, M. G. Kanatzidis, J. J. Crochet, J. Even, and A. D. Mohite, Nat. Commun. **9**, 2254 (2018).

[84] M. D. Smith, L. Pedesseau, M. Kepenekian, I. C. Smith, C. Katan, J. Even, and H. I. Karunadasa, Chem. Sci. **8**, 1960 (2017).

[85] M. L. Tiago, J. E. Northrup, and S. G. Louie, Phys. Rev. B **67**, 115212 (2003).

[86] D. Jacquemin, I. Duchemin, and X. Blase, J. Chem. Theory Comp. **11**, 3290 (2015).

[87] Computational Chemistry Comparison and Benchmark Data Base from National Institute of Standards and Technology available at https://cccbdb.nist.gov/gap1.asp.

[88] O. J. Weber, K. L. Marshall, L. M. Dyson, and M. T. Weller, Acta. Crystallogr. B **71**, 668 (2015).

[89] T. S. van der Poll, A. Zhugayevych, E. Chertkov, R. C. Bakus, J. E. Coughlin, S. J. Teat, G. C. Bazan, and S. Tretiak, J. Phys. Chem. Lett. **5**, 2700 (2014).

[90] S. Shao, J. Liu, G. Portale, H.-H. Fang, G. R. Blake, G. H. ten Brink, L. J. A. Koster, and M. A. Loi, Adv. Energy Mater. **8**, 1702019 (2017).

[91] X. Yang, X. Zhang, J. Deng, Z. Chu, Q. Jiang, J. Meng, P. Wang, L. Zhang, Z. Yin, and J. You, Nat. Commun. **9**, 570 (2018).

[92] K. Jemli, P. Audebert, L. Galmiche, G. Trippé-Allard, D. Garrot, J.-S. Lauret, and E. Deleporte, ACS Appl. Mater. Interfaces **7**, 21763 (2015).

[93] G. Kresse and J. Hafner, Phys. Rev. B **47**, 558 (1993).

[94] G. Kresse and J. Furthmüller, Comput. Mater. Sci. **6**, 15 (1996).

[95] G. Kresse and J. Furthmüller, Phys. Rev. B **54**, 11169 (1996).

[96] G. Kresse and D. Joubert, Phys. Rev. B **59**, 1758 (1999).

[97] J. P. Perdew and Y. Wang, Phys. Rev. B **45**, 13244 (1992).

[98] J. P. Perdew, A. Ruzsinszky, G. I. Csonka, O. A. Vydrov, G. E. Scuseria, L. A. Constantin, X. Zhou, and K. Burke, Phys. Rev. Lett. **100**, 136406 (2008).

[99] J. Even, L. Pedesseau, M.-A. Dupertuis, J.-M. Jancu, and C. Katan, Phys. Rev. B **86**, 205301 (2012).

[100] A. V. Krukau, O. A. Vydrov, A. F. Izmaylov, and G. E. Scuseria, J. Chem. Phys. **125**, 224106 (2006).

[101] H. Ehrenreich and M. H. Cohen, Phys. Rev. **115**, 786 (1959).

[102] G. Kresse, M. Marsman, and Furthmüller, VASP Manual, 2016, available at http://cms.mpi.univie.ac.at/vasp/vasp/vasp.html

[103] E. E. Salpeter and H. A. Bethe, Phys. Rev. **84**, 1232 (1951).

[104] M. Rohlfing and S. G. Louie, Phys. Rev. B **62**, 4927 (2000).

[105] G. Cappellini, R. Del Sole, L. Reining, and F. Bechstedt, Phys. Rev. B **47**, 9892 (1993).

[106] P. H. Hahn, W. G. Schmidt, and F. Bechstedt, Phys. Rev. Lett. **88**, 016402 (2001).

[107] W. G. Schmidt, S. Glutsch, P. H. Hahn, and F. Bechstedt, Phys. Rev. B **67**, 085307 (2003).

[108] C. Rödl, F. Fuchs, J. Furthmüller, and F. Bechstedt, Phys. Rev. B **77**, 184408 (2008).